

The switching location of a bipolar memristor: chemical, thermal and structural mapping

John Paul Strachan¹, Dmitri B Strukov², Julien Borghetti¹,
J Joshua Yang¹, Gilberto Medeiros-Ribeiro¹
and R Stanley Williams¹

¹ Nanoelectronic Research Group, Hewlett-Packard Labs, 1501 Page Mill Road, Palo Alto, CA 94304, USA

² Department of Electrical and Computer Engineering, University of California, Santa Barbara, Santa Barbara, CA 93106, USA

E-mail: strukov@ece.ucsb.edu and stan.williams@hp.com

Received 22 November 2010, in final form 20 January 2011

Published 16 May 2011

Online at stacks.iop.org/Nano/22/254015

Abstract

Memristors are memory resistors promising a rapid integration into future memory technologies. However, progress is still critically limited by a lack of understanding of the physical processes occurring at the nanoscale. Here we correlate device electrical characteristics with local atomic structure, chemistry and temperature. We resolved a single conducting channel that is made up of a reduced phase of the as-deposited titanium oxide. Moreover, we observed sufficient Joule heating to induce a crystallization of the oxide surrounding the channel, with a peculiar pattern that finite element simulations correlated with the existence of a hot spot close to the bottom electrode, thus identifying the switching location. This work reports direct observations in all three dimensions of the internal structure of titanium oxide memristors.

1. Introduction

The phenomenon of resistance switching in thin film devices has a long history of research [1–4] that has found new relevance [5] for developing a high density non-volatile universal memory as well as computational functionality beyond CMOS technology [6]. Additionally, the fourth fundamental passive circuit element, the memristor [7, 8], was shown to be physically realized with titanium dioxide bipolar resistance switching devices [9]. These motivations have driven significant advances in device development and materials research [10–15].

Recent work [16, 17] shows that TiO₂-based memristors contain phases with significant concentrations of oxygen vacancies. In the case of TiO₂ devices operated in a unipolar mode [16], the low resistance state of the device is composed of ~10 nm Ti₄O₇ metallic channels through an anatase film, while in the high resistance state these channels have dispersed. In bipolar operation, an initial electroforming step

creates a ~100 nm wide Ti₄O₇ channel, but no measurable material changes are observed during subsequent ON/OFF switching [17]. Electroforming of TiO₂ clearly involves a reduction process that generates oxygen vacancies, which can subsequently condense into a stable, ordered phase (e.g. Mágneli Ti₄O₇). The Ti₄O₇ phase is metallic at room temperature, but the strong nonlinear (tunneling) transport [18] of a bipolar device reveals that it is not entirely shorted by this channel. The ON/OFF switching then results from the modulation of a barrier between the channel and one of the electrodes, with estimates of the barrier width in the 1.5 ± 0.5 nm range [19]. Direct imaging of this gap modulation poses significant experimental challenges.

Here, we shed some light on the ON/OFF switching process, using both spectromicroscopic observations and modeling of the Joule heating present during switching. We examine the effects of this heating, particularly how it enables us to identify the ultimate location of the switching site following the electroforming.

2. Sample preparation and switching

Our memristive devices have a bottom electrode of Cr (5 nm)/Pt (18 nm), a top electrode of Pt (30 nm) and a switching layer of TiO₂ (25 nm). The stack is fabricated atop a thin 20 nm silicon nitride window having a $45 \times 45 \mu\text{m}^2$ area in which the underlying Si substrate (350 μm thick) has been etched away (see figure 3(a), left inset). The adhesion layer plays an important role in generating vacancies in the switching layer [20], but Cr was used rather than the more strongly reducing Ti to avoid introducing a background Ti signal in the subsequent spectromicroscopy work. The bottom and top Pt electrodes were patterned by photolithography, resulting in a width of 1.7 and 1.5 μm , respectively. The TiO₂ layer was unpatterned, extending across the substrate. The as-grown film was determined to be amorphous by x-ray and electron diffraction measurements [18, 21]. This device has an identical materials stack, fabrication process and electrical switching behavior to that in [17]. Thus, much of the understanding from previous electrical and material studies of window devices can be applied to and expanded upon in this study, and are frequently referenced here. However, note that these devices differ from those of other studies [22] in that the device is not entirely heat-sunked at the bottom to a bulk substrate, such as a silicon wafer. Additionally, the lithographic processing of the electrodes, including an oxygen descum and the use of a Cr adhesion layer, leads ultimately to a non-ohmic bottom contact in this case (see below).

The memristive device after fabrication (virgin state) was highly insulating, with the current–voltage (I – V) curve showing a strong rectifying behavior similar to devices prepared on a bulk substrate, shown in figure 1(a) (inset). This has been interpreted in terms of a Schottky-like contact at the top and bottom interfaces, with a smaller barrier at the bottom due to the diffusion of adhesion-layer metal atoms that can partially reduce that interface [20]. An electroforming step was performed with a strong negative bias applied to the top electrode with the bottom electrode grounded (figure 1(a)). This step enabled the resistance switching that followed, although it has been shown that this step can be eliminated for bipolar TiO₂-based memristors by growing devices with a layer that is intentionally doped with vacancies [22].

Following the electroforming, one cycle of bipolar switching was performed (figure 1(b)). During this cycle, there was substantial heating, as directly measured using a simple thermometry method as in [18]. Here, since four-probe electrical measurements were made during the switching, we can correlate a small increase in the resistance of the electrodes themselves with a temperature rise in the electrodes. The average temperature rise in the bottom electrode at each step in the switching is shown in the coloring of the current–voltage traces in figure 1(b). The color scale is linear with resistance increase and thus with the average temperature in the electrode, and was determined to be linear with the power. The maximum heating in the electrode, a temperature increase of roughly 5.7 K, occurred at the points of switching in figure 1(b).

We can further quantify the temperature profile during switching inside the junction. Since the power dissipated along

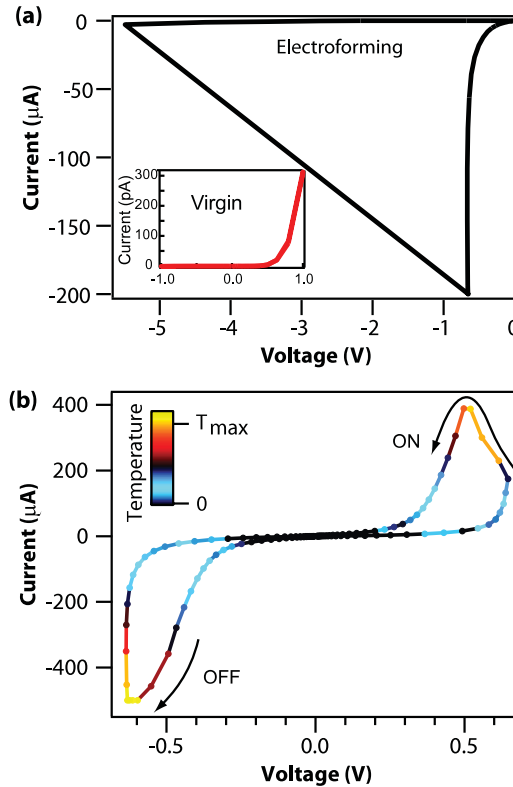


Figure 1. Electroforming and switching of a Pt/TiO₂/Pt crossbar device fabricated atop a thin silicon nitride membrane. (a) A highly resistive initial state (inset) is swept to an external voltage of -7 V , in which a soft breakdown in a localized region of the device generates vacancies and allows the subsequent switching. (b) Following electroforming, the device is cycled ON and OFF exactly one time using a four-probe geometry. The trace coloring gives the electrode temperature simultaneously measured by the resistance increase due to Joule heating (see description in main text). The highest local junction temperature is estimated (see text) to reach $T_{\text{max}} \approx 665 \text{ K}$.

the electrodes themselves was negligible, we can ignore Joule heating in the electrodes and assume that the heating source was localized within the crossbar junction. We also assume that significant temperature increases can only occur on the silicon nitride membrane, while outside the $45 \times 45 \mu\text{m}^2$ window area (see figure 3(a), left inset) the silicon substrate, being thick and a good heat conductor, serves as a strong heat sink. Thus, the 5.7 K average temperature increase across the length of the electrode reflects a substantially hotter temperature in the junction itself. We performed finite difference numerical simulations for stationary heat transfer and determined the dependence of the maximum increase of the temperature in the structure (i.e. at the center of the heat source) as a function of the average temperature increase in the electrode. The resulting relation was $\Delta T_{\text{MAX}} \approx 2.55 \langle \Delta T_E \rangle$. Accounting for the fact that the membrane portion of the bottom electrode is only 1/25 of the entire electrode length, $\langle \Delta T_{\text{BE}} \rangle \approx 25 (R_{\text{BE}}(\text{high bias})/R_{\text{BE}}(\text{zero bias}) - 1)/\alpha$, where $\alpha = 1.2 \times 10^{-3} \text{ K}^{-1}$ is the temperature coefficient of Pt for similar electrodes measured in [18]. From this, a peak

temperature T_{MAX} within the junction is estimated to be 665 K, which is higher than the crystallization temperature of the amorphous TiO_2 thin film [23] and is thus expected to induce an amorphous to crystalline transition.

Such heating during switching has been observed previously [17, 18], and is further investigated below. In contrast to the ON/OFF switching, the amount of heating measured during the electroforming step was substantially less (roughly half), and in identical devices we have observed that electroforming alone does not induce crystallization of amorphous TiO_2 (see [17], supplementary information).

3. X-ray spectromicroscopy

Following electroforming and one cycle of switching, the memristive device was loaded into the scanning transmission x-ray microscope (STXM) at the Advanced Light Source, which is a soft x-ray bending magnet beamline with 35 nm spatial resolution given by a Fresnel zone plate and 70 meV energy resolution [24]. Spatially resolved x-ray absorption experiments were then performed through the 20 nm silicon nitride windows with crossbar devices on top.

The device junction area was imaged in STXM, as shown in figure 2(a). By sweeping the incident x-ray energy and measuring the fine structure of the Ti $L_{2,3}$ absorption spectrum, different material states of the titanium oxide layer buried within the electrodes can be identified in a non-destructive manner [25, 26]. Consistent with earlier x-ray spectromicroscopy of TiO_2 memristors [17], figure 2(b) shows the Ti spectra for three phases observed in the device: amorphous, anatase and a partially reduced sub-oxide. The location of the three phases was spatially mapped and color coded green, red and blue, respectively, by acquiring the Ti $L_{2,3}$ spectrum at each pixel, as shown in figure 2(c). The as-grown amorphous phase (green) dominates, except in a region at the bottom left corner of the junction. As shown, a circular sub-oxide channel was observed here (blue in figure 2(c)) with ~ 100 nm diameter. Selected-area electron diffraction (SAED) and high resolution TEM measurements in this region did not reveal any structurally ordered phase within the higher conductivity channel, unlike in [17]. Around this channel, an anatase phase was observed (red in figure 2(c)). For this thickness film, the formation of the anatase phase is known to occur by annealing the initially amorphous film above ~ 625 K [23]. The only form of heating present in this device was Joule heating through the device itself during forming and the single switching cycle, and thus the presence of the anatase phase surrounding the sub-oxide channel confirms that this channel carried the electrical current.

The heating pattern observed in figure 2(c) around the sub-oxide conductive channel provides a unique opportunity to better understand the ON/OFF switching in the bipolar operating mode of TiO_2 devices. An important observation is the half-circle shape of the heated region. The anatase phase is only observed to be present above the bottom electrode in figure 2(c), while one might expect the Joule heating from the sub-oxide channel to uniformly heat a circular

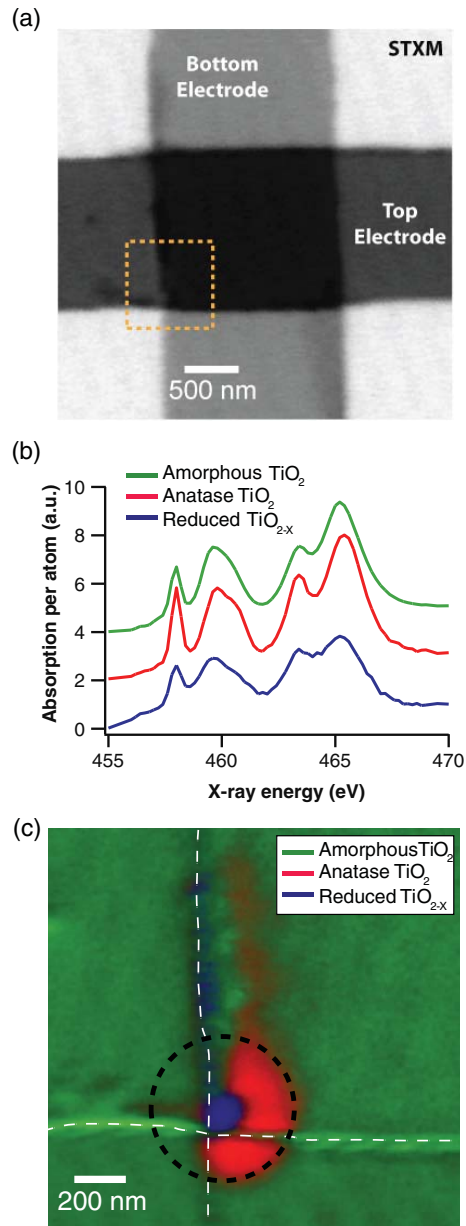


Figure 2. Physical characterization of a cycled Pt/ TiO_2 /Pt device. (a) STXM image of the device junction area, taken at an x-ray energy of 445.0 eV. The bottom and top electrodes are labeled, as well as an area within the device which was scanned at higher resolution. (b) Ti $L_{2,3}$ x-ray absorption spectra (normalized by the post-edge intensity giving absorption per atom) showing three material states present within the device in different spatial locations: amorphous, anatase and reduced. (c) Higher resolution scan of the bottom left corner of the junction with a spatial mapping of the three observed phases of titanium oxide present. The color mapping of these regions is derived from the Ti $L_{2,3}$ x-ray absorption image stack using singular value decomposition procedures. A circle identifies the expected heated region surrounding the conductive channel (see text).

pattern around the channel (dashed circle in figure 2(c)). In the following section, we argue that this semicircle pattern developed because of the specific location of the channel

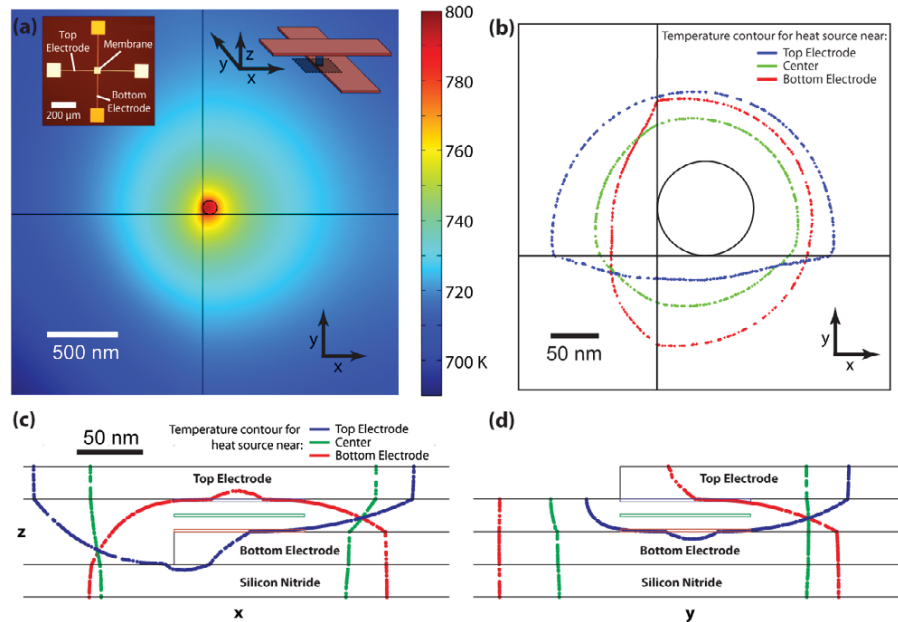


Figure 3. Three-dimensional steady-state heat transfer simulation. (a) Temperature map for an x - y slice taken through the middle of a 2 nm high and 100 nm wide cylindrical uniform heat source located directly on top of the bottom electrode (i.e. 1 nm above the surface of the bottom electrode, illustrated in right inset). Left inset shows a top view of the full device including membrane window. (b) Temperature contours for $T = 760$ K along x - y slices for three different positions of heat source: directly on top of the bottom electrode (red, and the same as in panel a); exactly between top and bottom electrode (green) and directly below top electrode (blue). The x - y position for the cylindrical heat source is the same for all cases and shown with a black circle in both panels. (c) and (d) Similar temperature contours along an x - z slice (c) and y - z slice (d) going through the center of the conductive channel for three different positions of heat source. The heat source position in each case is indicated by the colored rectangle within the junction.

gap and therefore identifies the location at which ON/OFF switching occurred.

4. Thermal modeling

To understand how the specific asymmetric heating pattern (half-circle in figure 2(c)) can arise in our device geometry during bipolar switching, we performed coupled electro-thermal finite element analysis using COMSOL [27]. More specifically, full three-dimensional steady-state heat flow simulations were carried out on a model of the entire membrane area ($45 \times 45 \mu\text{m}^2$) with material dimensions matching the device and thermal conductivities of 3, 10 and $70 \text{ W m}^{-1} \text{ K}^{-1}$ assumed for the TiO_2 , silicon nitride, and Pt, respectively. The thick silicon substrate acted as a heat sink, so the perimeter of the membrane was assumed to be at the fixed temperature $T = 300$ K, while heat transfer between the ambient and the top and bottom surfaces of the membrane was neglected. Even though the dimensions of the membrane were rather large, steady-state simulations were adequate because of the relatively slow voltage sweep rate for collecting experimental data. For example, the thermal time constant for the entire window and device structure was determined to be $10 \mu\text{s}$, while there was about 2 ms between adjacent data points in figure 1(b).

All heating was assumed to come from the conductive channel in the junction. In our case I - V s in both the OFF

and ON states were nonlinear over the entire voltage range, so it is safe to assume that all the applied bias dropped across a tunnel barrier [18] and that is where Joule heating mostly occurred. The maximum power level of $300 \mu\text{W}$ dissipated in the channel during switching was determined from figure 1(b) (i.e. for $V = -0.6$ V and $I = -500 \mu\text{A}$), and the spatial position and cross-sectional area of the conductive channel was derived from figure 2(c). We modeled the heat source as a 2 nm high (i.e. tunnel barrier width) and 100 nm diameter (from figure 2(c)) cylindrical heat source. For simplicity, we assumed that the power was dissipated uniformly inside the heat source.

A key question answered in the affirmative by these simulations was whether the precise placement of the heating source within the titanium oxide layer (in the z direction, see figure 3(a), right inset) would have a significant effect on the temperature profile, and ultimately the region of crystallized TiO_2 . Figure 3(a) shows the temperature map along an x - y planar slice (parallel to the sample surface) taken through the middle of the cylindrical heat source placed directly on top of the bottom electrode. This slice revealed the highest temperature upon heating, and was therefore of interest since the crystallization kinetics is exponentially dependent on temperature. The temperature profile was clearly asymmetric and followed the bottom electrode for the higher temperatures, i.e. producing a semicircle shape.

To further check this observation (and, for example, to rule out the effect of the silicon nitride membrane), the temperature

profile was simulated for two other cases: when the same heat source was located in the middle of the film (exactly between the top and bottom electrodes), and just below the top electrode. Figure 3(b) shows the temperature contours for these cases. The temperature profiles in both cases were very different: roughly symmetric (green) or following the top electrode (blue). This is further illustrated by the temperature contours in the x - z and y - z planes, shown in figures 3(c) and (d), respectively. Although the absolute value of the temperatures may vary based upon the values chosen for the thermal conductance of the various components, the shapes of the profiles are independent of the quantitative details and thus our conclusion about the location of the heating is robust.

5. Discussion

Our observation of an insulating or tunneling gap at the bottom interface is consistent with the electroforming step of figure 1(a). While the microscopic details remain controversial, it is generally accepted that electroforming involves a ‘soft breakdown’ including processes of electrochemical reduction [21], heating and field-driven bond rupturing [28, 29] ultimately creating a conductive channel across the TiO₂ layer. The polarity of the bias applied during electroforming will set the orientation of the conductive channel. In our case, the virgin device (figure 1(a), inset) was rectifying at the top interface, and a negative bias was applied to the top electrode with the bottom electrode grounded. The strong electric field across the material may initiate the electroforming by rupturing chemical bonds in the material and forming a favorable path for the flow of current and vacancies, according to thermochemical dielectric breakdown theory [28]. Electrochemical reduction processes led to the creation of positively charged oxygen vacancies at the anode (bottom electrode), which drift up towards the top electrode due to the electric field, effectively piling up near and shunting the rectifying top interface. A vacancy-rich conductive channel will continue to grow from the top electrode down towards the bottom electrode until the remaining gap becomes small enough to conduct current and the reduced voltage drop is insufficient to continue the electroforming. The result is a gap at the bottom interface, which was the location for the subsequent ON/OFF switching [19] for the device reported here.

While this work has revealed that switching occurs near the bottom interface of the device examined in this study, previous studies [22] have shown the opposite result, namely switching controlled by the top interface. The reason for this difference is that the present device, as noted earlier, involved lithographic processing of the electrodes and a weakly reducing Cr adhesion layer, both of which contributed to a non-ohmic bottom interface barrier that is switchable. In contrast, the devices of [22] were strongly ohmic at the bottom contact, making it nearly impossible to electrically modulate this interface. Instead, switching occurs at the non-ohmic top interface. These differences are further highlighted by the switching polarity of the respective devices, namely ON (OFF) switching with positive (negative) bias applied to the

top electrode, whereas for the switching polarity in [22], the ON (OFF) switching was induced by negative (positive) bias on the top electrode.

6. Conclusion

After electroforming and one switching cycle of a metal/TiO₂/metal memristor, we directly observed a \sim 100 nm conducting channel that we identified to be oxygen-deficient (vacancy-rich) relative to the deposited material. No structural order was found in this channel, unlike in [17], suggesting that composition (Ti to O ratio) is more crucial than long-range order in enabling resistance switching in titanium oxide. We observed a heat-induced transformation of amorphous TiO₂ into an anatase phase around the channel, confirming that the channel was the conductor of current in the device. By comparing the semicircular shape and orientation of the observed anatase in the device with finite element simulations of the temperature profile caused by Joule heating, we deduced that the heating source was adjacent to the bottom electrode during switching. This also provided evidence that heating of the insulating gap between the tip of the conductive channel and the bottom electrode assisted the kinetics of the switching process.

Acknowledgments

We thank A L D Kilcoyne, X Li, D A A Ohlberg and T Tran for experimental assistance. Work at HP is sponsored by the US Government’s Nano-Enabled Technology Initiative. Work at the Advanced Light Source, Lawrence Berkeley National Laboratory is supported by the Director, Office of Science, Office of Basic Energy Sciences, of the US Department of Energy under contract no. DE-AC02-05CH11231. Work at UCSB is partially funded by Air Force Office of Scientific Research under contract no. DE-AC02-05CH11231, and by a grant from HP Labs Palo Alto.

References

- [1] Dearnaley G, Stoneham A M and Morgan D V 1970 *Rep. Prog. Phys.* **33** 1129
- [2] Waser R, Dittman R, Staikov G and Szot K 2009 *Adv. Mater.* **21** 2632
- [3] Sawa A, Fuji T, Kawasaki M and Tokura Y 2004 *Appl. Phys. Lett.* **85** 4073
- [4] Schindler C, Therman S C P, Waser R and Kozicki M N 2007 *IEEE Trans. Electron Devices* **54** 2762
- [5] Liu S Q, Wu N J and Ignatiev A 2000 *Appl. Phys. Lett.* **76** 2749
- [6] Borghetti J, Snider G S, Kuekes P J, Yang J J, Stewart D R and Williams R S 2010 *Nature* **464** 873
- [7] Chua L O 1971 *IEEE Trans. Circuit Theory* **18** 507
- [8] Chua L O and Kang S M 1976 *Proc. IEEE* **64** 209
- [9] Strukov D B, Snider G S, Stewart D R and Williams R S 2008 *Nature* **453** 80
- [10] Szot K, Speier W, Bihlmayer G and Waser R 2006 *Nat. Mater.* **5** 312
- [11] Janousch M, Meijer G I, Staub U, Delley B, Karg S F and Andreasson B P 2007 *Adv. Mater.* **19** 2232
- [12] Meijer G I 2008 *Science* **319** 1625
- [13] Odagawa A 2004 *Phys. Rev. B* **70** 224403

- [14] Rozenberg M J, Inoue I H and Sánchez M J 2006 *Appl. Phys. Lett.* **88** 033510
- [15] Jeong D S, Schroeder H and Waser R 2009 *Phys. Rev. B* **79** 195317
- [16] Kwon D-H *et al* 2010 *Nat. Nanotechnol.* **5** 148
- [17] Strachan J P, Pickett M D, Yang J J, Aloni S, Kilcoyne A L D, Medeiros-Ribeiro G and Williams R S 2010 *Adv. Mater.* **22** 3573
- [18] Borghetti J, Strukov D B, Pickett M D, Yang J J, Stewart D R and Williams R S 2009 *J. Appl. Phys.* **106** 124504
- [19] Pickett M D, Strukov D B, Borghetti J L, Yang J J, Snider G S, Stewart D R and Williams R S 2009 *J. Appl. Phys.* **106** 074508
- [20] Yang J J, Strachan J P, Xia Q, Ohlberg D A A, Kuekes P J, Kelley R D, Stickle W F, Stewart D R, Medeiros-Ribeiro G and Williams R S 2010 *Adv. Mater.* **22** 4034
- [21] Yang J J, Pickett M D, Li X, Ohlberg D A A, Stewart D R and Williams R S 2008 *Nat. Nanotechnol.* **3** 429
- [22] Yang J J, Miao F, Pickett M D, Ohlberg D A A, Stewart D R, Lau C N and Williams R S 2009 *Nanotechnology* **20** 215201
- [23] Strachan J P, Yang J J, Münstermann R, Scholl A, Medeiros-Ribeiro G, Stewart D R and Williams R S 2009 *Nanotechnology* **20** 485701
- [24] Kilcoyne A L D *et al* 2003 *J. Synchrotron Radiat.* **10** 125
- [25] Stöhr J 1992 *NEXAFS Spectroscopy* (Berlin: Springer)
- [26] Ade H and Stoll H 2009 *Nat. Mater.* **8** 281
- [27] COMSOL multiphysics modeling software <http://www.comsol.com>
- [28] McPherson J, Kim J-Y, Shanware A and Mogul H 2003 *Appl. Phys. Lett.* **82** 2121
- [29] O'Dwyer J J 1969 *J. Electrochem. Soc.* **116** 239